

Article

Effect of the Surface Film Formed by Hydrogen Charging on the Corrosion Behavior of an As-Cast Mg–8%Li (in wt. %) Alloy

 Shuo Wang ^{1,2,3}, Daokui Xu ^{2,4,5,*} , Baojie Wang ^{6,*}, Dongliang Wang ², Zhiqiang Zhang ^{1,3,*} and Xiangbo Xu ²
¹ Key Lab of Electromagnetic Processing of Materials, Ministry of Education, Northeastern University, Shenyang 110819, China; wangs1909@foxmail.com

² Key Laboratory of Nuclear Materials and Safety Assessment, Institute of Metal Research, Chinese Academy of Sciences, Shenyang 110016, China; dlwang19s@imr.ac.cn (D.W.); xiangbo@zju.edu.cn (X.X.)

³ Engineering Research Center of Advanced Materials Preparing Technology, Ministry of Education, Northeastern University, Shenyang 110819, China

⁴ Binzhou Institute of Technology, Binzhou 256606, China

⁵ Shandong Key Laboratory of Advanced Aluminium Materials and Technology, Binzhou 256606, China

⁶ School of Environmental and Chemical Engineering, Shenyang Ligong University, Shenyang 110159, China

* Correspondence: dkxu@imr.ac.cn (D.X.); bjwang@alum.imr.ac.cn (B.W.); zqzhang@mail.neu.edu.cn (Z.Z.)

Abstract: In this study, the effect of electrochemical hydrogen charging on the corrosion behavior of an as-cast Mg–8%Li alloy was investigated. It was revealed that after being cathodically hydrogen charged in a 0.1 M NaCl solution at a constant current density of 50 mA/cm² for 3 h, a product film with an average thickness of 20 μm was formed in the α-Mg phase, whilst the average thickness of the product film being formed in the β-Li phase was 6 μm. When the charging time was prolonged to 18 h, the thicknesses of the product films being formed on the α-Mg and β-Li phases were increased to 75 and 20 μm, respectively. The results of the grazing incidence X-ray diffraction (GIXRD) testing showed that the product films of the differently charged samples mainly consisted of Mg(OH)₂, LiOH and Li₂CO₃. The formed product films on the two matrix phases were dense and could hinder the erosion of Cl[−] in a solution, and hence improved the corrosion resistance of the alloy. After being hydrogen charged for 3 h, the charge-transfer resistance (R_{ct}) value of the alloy was increased from 527 to 1219 Ω·cm². However, when the hydrogen charging time was prolonged to 18 h, the R_{ct} was slightly reduced to 1039 Ω·cm² due to the cracking of the surface product films and the interfacial cracking of the film/substrate matrix.

Keywords: magnesium–lithium alloy; hydrogen charging; product film; corrosion behavior



Citation: Wang, S.; Xu, D.; Wang, B.; Wang, D.; Zhang, Z.; Xu, X. Effect of the Surface Film Formed by Hydrogen Charging on the Corrosion Behavior of an As-Cast Mg–8%Li (in wt. %) Alloy. *Coatings* **2023**, *13*, 800. <https://doi.org/10.3390/coatings13040800>

Academic Editor: Frederic Sanchette

Received: 22 March 2023

Revised: 4 April 2023

Accepted: 14 April 2023

Published: 20 April 2023



Copyright: © 2023 by the authors. Licensee MDPI, Basel, Switzerland. This article is an open access article distributed under the terms and conditions of the Creative Commons Attribution (CC BY) license (<https://creativecommons.org/licenses/by/4.0/>).

1. Introduction

As one of the lightest metallic structural materials, magnesium–lithium (Mg–Li) alloys have the high potential for reducing the weight of equipment and saving energy in industrial fields [1–5]. Generally, the mass fraction of Li determines the crystallographic structures of Mg–Li alloys [6]. Figure 1 shows the binary phase diagram of Mg–Li alloys calculated by Pandat software (CompuTherm LLC, Madison, WI, USA, version 8.0). It reveals that when the addition of Li ranges from 5.7 to 10.3 wt. %, the matrix of the Mg–Li alloys has a dual-phase structure with hexagonal close-packed (HCP) structured α-Mg and body-centered cubic (BCC) structured β-Li phases. Since dual-phase Mg–Li alloys usually have moderate mechanical strength, excellent ductility and good deformability, their development prospects in the aerospace, weapon and automotive industries are promising [7–11]. However, since the chemical activities of Mg and Li are high, the anodic dissolution of Mg–Li alloys can easily occur in aqueous environments and simultaneously cause hydrogen evolution [12–15]. It has been widely reported that hydrogen could influence the service properties of Mg alloys, such as the mechanical properties [16–28] and corrosion resistance [17–19,29–33]. For dual-phase structured Mg–Li alloys, Wang et al. [33]

reported that hydrogen charging could simultaneously deteriorate the tensile strength and ductility of an as-cast Mg–8%Li (in wt. %) alloy. However, few relevant investigations about the influence of hydrogen on the corrosion performance of Mg–Li alloys could hitherto be referenced. Song et al. [32] reported that for a Mg–2Zn alloy being hydrogen charged at 10 mA for 2 h in a 0.1 M NaCl solution, the measured corrosion current density (i_{corr}) was decreased by 80%. The higher corrosion resistance of the hydrogen-charged sample originated from the barrier effect of a compacter Mg(OH)₂ film being formed on the sample surface [32]. Similarly, Wang et al. [17] reported that for an as-cast Mg–7%Gd–5%Y–1%Nd–0.5%Zr alloy being hydrogen charged at -27.8 mA/cm^2 for 1 h in a 3.5 wt. % NaCl solution, an obvious surface product film could be formed. However, since the Mg₅Gd phase had a higher corrosion potential than the α -Mg matrix, the driving force for hydrogen evolution in the Mg₅Gd phase was stronger than that in the α -Mg phase under the same applied cathodic charging potential. This resulted in severe hydrogen-induced damages in the Mg₅Gd phases and then a deterioration of the protectiveness of the surface product film [17]. Similarly, for the Mg–8%Li alloy being conducted hydrogen charging at 50 mA/cm^2 for 3 h, obvious product films were also formed on the surface in the α -Mg and β -Li phases [33]. However, since the corrosion potentials in the α -Mg and β -Li phases were $-1.75 \text{ V}_{\text{SCE}}$ and $-2.38 \text{ V}_{\text{SCE}}$ [34], respectively, the driving force for hydrogen evolution in the α -Mg phase was stronger under the same applied hydrogen charging potential and the hydrogen-induced damage mainly presented in the α -Mg phase [33]. Li et al. [6] reported that for a dual-phase structured Mg–7.5%Li alloy immersed in a NaCl solution, the film formed in the β -Li phase had good protectiveness and could effectively prevent the corrosion attack of Cl[−] anions. However, whether or not the product films that formed due to hydrogen charging could provide a similar protective effect on the dual-phase structured Mg–Li alloys requires further investigation.

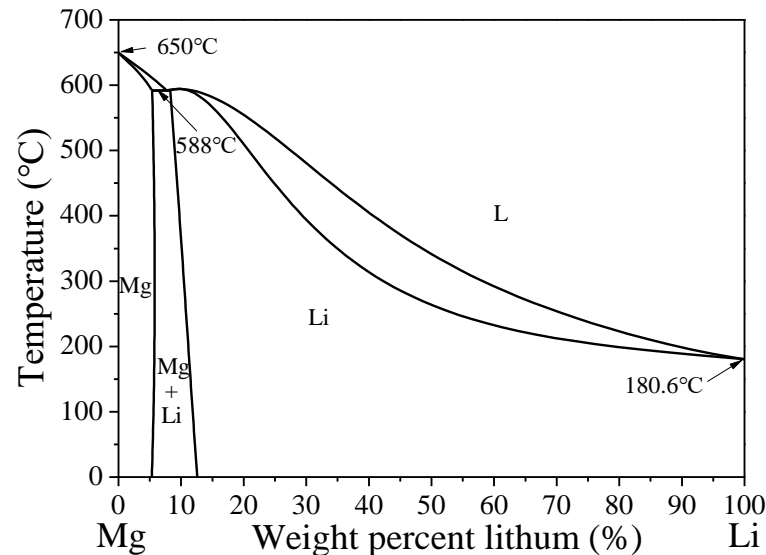


Figure 1. Binary phase diagram of Mg–Li alloys.

On the basis of the descriptions mentioned above, two questions can be proposed: (1) How do the product films formed by hydrogen charging influence the corrosion resistance of dual-phase structured Mg–Li alloys? (2) Do the product films prevent the α -Mg and β -Li phases from corrosion attack? In this study, these proposed questions are answered through an investigation of the corrosion behavior of an as-cast Mg–8%Li (in wt. %) alloy being electrochemically hydrogen charged for different durations of time. Moreover, the protection mechanism of the product film in the two matrix phases is discussed.

2. Materials and Methods

2.1. Material Preparation and Homogenization Treatment

The investigated material was an as-cast Mg–8%Li alloy, which was smelt in a vacuum resistance furnace under protective argon gas. After casting, the ingot with a dimension of 300 mm × 250 mm × 40 mm was obtained. Then, the ingot was held at 400 °C for 2 h to homogenize the microstructure. Using an inductively coupled plasma–atomic emission spectrum (ICP–AES) (Agilent, Beijing, China) apparatus, the determined chemical composition of the alloy was 8.2 wt. % Li and Mg balance. Moreover, the density and mechanical properties of the as-cast Mg–8%Li alloy were measured and listed in Table 1.

Table 1. Density and mechanical properties of the as-cast Mg–8%Li alloy.

Density (g/cm ³)	Yield Tensile Strength (MPa)	Ultimate Tensile Strength (MPa)	Elongation Ratio to Failure (%)
1.52 ± 0.04	65 ± 5	110 ± 5	38.5 ± 1.5

2.2. Microstructural Analysis

Samples with a dimension of 10 mm × 10 mm × 10 mm were sliced from the ingot. The sample surface was mechanically ground to a 5000-grit SiC paper first and then polished using diamond polishing paste to a 1.0 μm roughness. Thereafter, the polished surface was cleaned with alcohol and dried in air. X-ray diffraction (XRD; D/Max 2400) (Rigaku, Tokyo, Japan) was used for the phase analysis and scanning electron microscopy (SEM; EmCrafts CUBE II) (EmCrafts, Hanam-si, South Korea) was adopted to observe the microstructure.

2.3. Cathodic Hydrogen Charging Testing

Samples for cathodic hydrogen charging testing were connected to thin copper wires with conductive adhesive and mounted with epoxy resin. One surface with an area of 1 cm² was left exposed. Samples were polished to a 1.0 μm finish and then electrochemically hydrogen charged in a 0.1 M NaCl solution for 3, 6 and 18 h at a constant cathodic current density of 50 mA/cm² (yielding an electrode potential of approximately −4.50 V_{SCE}). The applied current density was consistent with previous studies [21,33]. All hydrogen charging tests were carried out using an electrochemical workstation (CorrTest CS350) (CorrTest, Wuhan, China) with a classical three-electrode system in which the reference electrode was the saturated calomel electrode (SCE) and the counter electrode was the Pt electrode. To clearly observe the formed surface product films, surface and three-dimensional (3D) morphologies of differently charged samples were observed using an optical microscope (OM; Keyence VHX 2000) (Keyence, Osaka, Japan) and their cross sections were observed using SEM. Moreover, a glancing incidence X-ray diffractometer (GIXRD; D/Max 2400) (Rigaku, Tokyo, Japan) under a glancing angle of 0.5° was used to analyze the compositions of product films. Compared with the X-ray photoelectron spectroscopy (XPS) method, the GIXRD method could be more suitable for determining whether the hydrates (such as LiOH·H₂O) were contained in the product films [35].

2.4. Electrochemical Measurements

Electrochemical measurements for the differently charged samples were pursued in 0.1 M NaCl solution and the electrochemical workstation (CorrTest CS350) (CorrTest, Wuhan, China) with the same three-electrode system mentioned in Section 2.3 was used. The potentiodynamic polarization tests were scanned from −250 mV_{SCE} to 350 mV_{SCE} versus open-circuit potential (OCP) at a scanning rate of 0.1667 mV/s after being stabilized for 600 s at OCP. After the potentiodynamic polarization tests, the obtained curves were fitted using CorrView software (CorrTest, Wuhan, China, version 3.1c). Electrochemical impedance spectroscopy (EIS) measurements were conducted at OCP after 600 s stabilization with a sinusoidal potential destabilization of 5 mV and a frequency ranging from

100 kHz to 0.01 Hz. The obtained EIS data were fitted using Zsimpwin 3.30d software (Ametek, San Diego, CA, USA, version 3.30d).

2.5. Hydrogen Evolution and Immersion Testing

To observe the changes in hydrogen evolution volume for the sample being immersed in the 0.1 M NaCl solution, the hydrogen-charged samples were mounted with epoxy resin and only one surface with an area of 1 cm² was left exposed. Then, the mounted samples were immersed for up to 48 h at room temperature. During the testing, in order to guarantee the stable pH of the experimental environment, the solution volume was about 200 times larger than the sample volume. Furthermore, the solution was renewed every 24 h and possessed a stable pH value of about 6.7 ± 0.2 , measured from a digital pH meter (INESA PHS-25) (INESA, Shanghai, China). To disclose the effect of hydrogen charging on the corrosion mechanism of the alloy, the macro corrosion morphologies of the uncharged and 3 h charged samples being immersed in 0.1 M NaCl solution for 0~48 h were observed using OM. Moreover, highly magnified and 3D observations of the corrosion morphologies in the uncharged and 3 h charged samples being immersed for 2, 4 and 8 h, respectively, were observed in situ using OM.

3. Results

3.1. Microstructural Characterization

Figure 2 shows the initial microstructure of the Mg–8%Li alloy. The XRD pattern exhibited that the alloy mainly consisted of α -Mg and β -Li phases (Figure 2a). The backscatter electron (BSE) image showed that the alloy had a dual-phase structure (Figure 2b). Figure 3 exhibits the surface and 3D morphologies of differently charged samples. On the basis of the 3D morphologies, it could be seen that the maximum surface height difference in the uncharged sample was 0.99 μm (Figure 3b). For the 3 h charged sample, an obvious white product film could be observed in the α -Mg phase and the surface in the β -Li phase was uniformly covered with a layer of dark product film (Figure 3c). Moreover, the maximum surface height difference was increased to 36.09 μm (Figure 3d). For the 6 h charged sample, the damage to the α -Mg phase became much more severe and the maximum surface height difference was increased to 54.78 μm (Figure 3e,f). After being charged for 18 h, the formed product film almost covered the whole sample surface and the maximum surface height difference increased to 100.60 μm (Figure 3g,h).

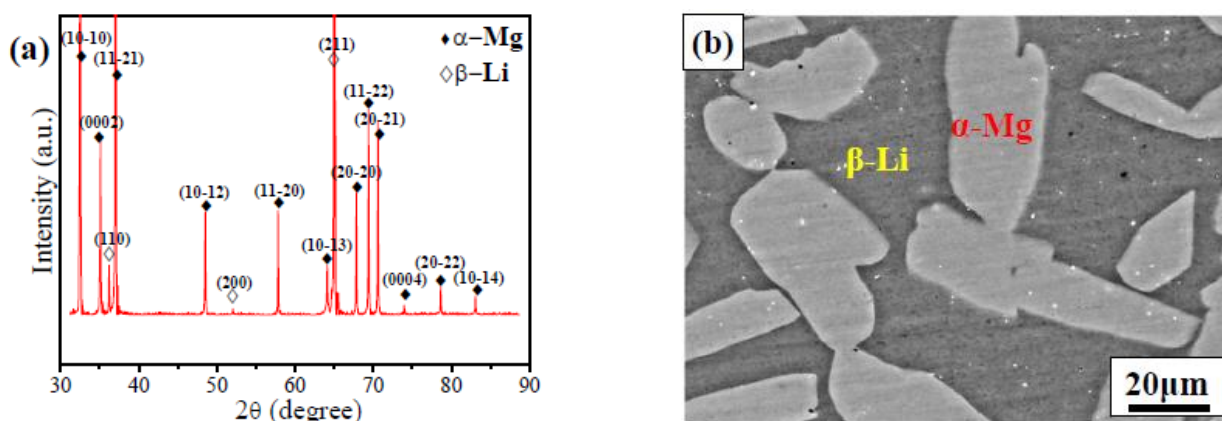


Figure 2. Microstructural characterization of the as-cast Mg–8%Li alloy: (a) XRD pattern, (b) BSE image.

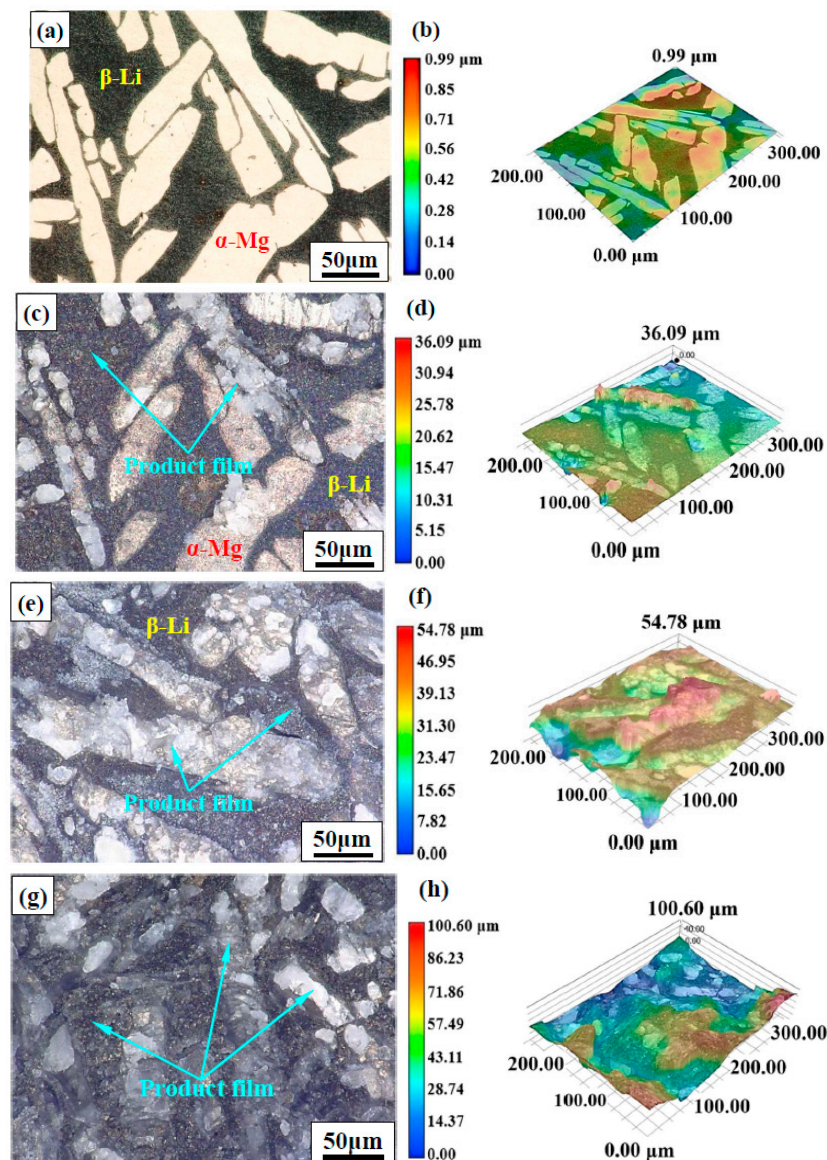


Figure 3. Surface and 3D morphologies of different samples after being hydrogen charged for: (a) 0 h, (c) 3 h, (e) 6 h and (g) 18 h. Images (b), (d), (f) and (h) are the corresponding 3D morphologies of images (a), (c), (e) and (g), respectively.

The GIXRD patterns in the formed product films are shown in Figure 4. For the 3 h, 6 h and 18 h charged samples, the product films were mainly constituted of $\text{Mg}(\text{OH})_2$, LiOH and Li_2CO_3 . Figure 5 presents the cross-sectional morphologies of the charged samples. It could be seen that for the 3 h charged sample, the average thickness of the product film formed in the α -Mg phase was 20 μm , whilst that in the β -Li phase was about 6 μm (Figure 5a,b). Moreover, the product films in the two phases were relatively uniform and only several microcracks could be seen in the product films (Figure 5b). The energy dispersive spectrum (EDS) results demonstrated that the product film in the α -Mg phase mainly contained Mg and O, whereas the main elements of the film in the β -Li phase were Mg, O and C (Figure 5b). With the prolongation of the hydrogen charging time, the thicknesses of the product films in the two phases were gradually increased (Figure 5c–f). For the 6 h charged sample, the average thickness of the product film formed in the α -Mg phase was about 40 μm and that in the β -Li phase was 10 μm (Figure 5c,d). Meanwhile, the number of cracks present in the interior of the product films increased (Figure 5d). Moreover, cracks could also be formed at the interfaces of the product film/substrate phases

(Figure 5d). In the 18 h charged sample, the average thickness values of the product films in the α -Mg and β -Li phases were further increased to 75 and 20 μm , respectively (Figure 5e,f). Furthermore, the number of cracks being presented in the interior of the product films and at the interfaces of the product film/substrate phases was further increased (Figure 5f).

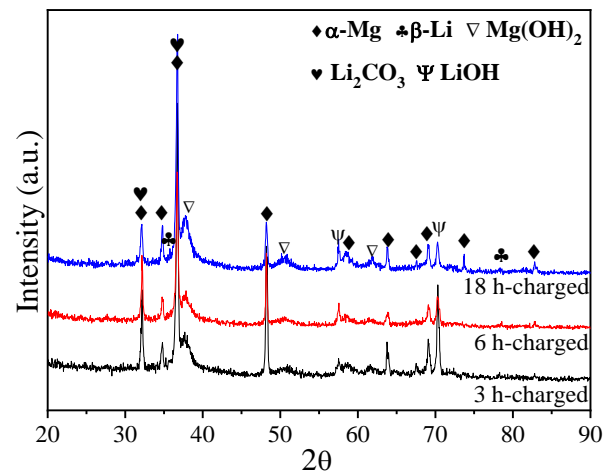


Figure 4. GIXRD patterns of the formed product films for differently charged samples.

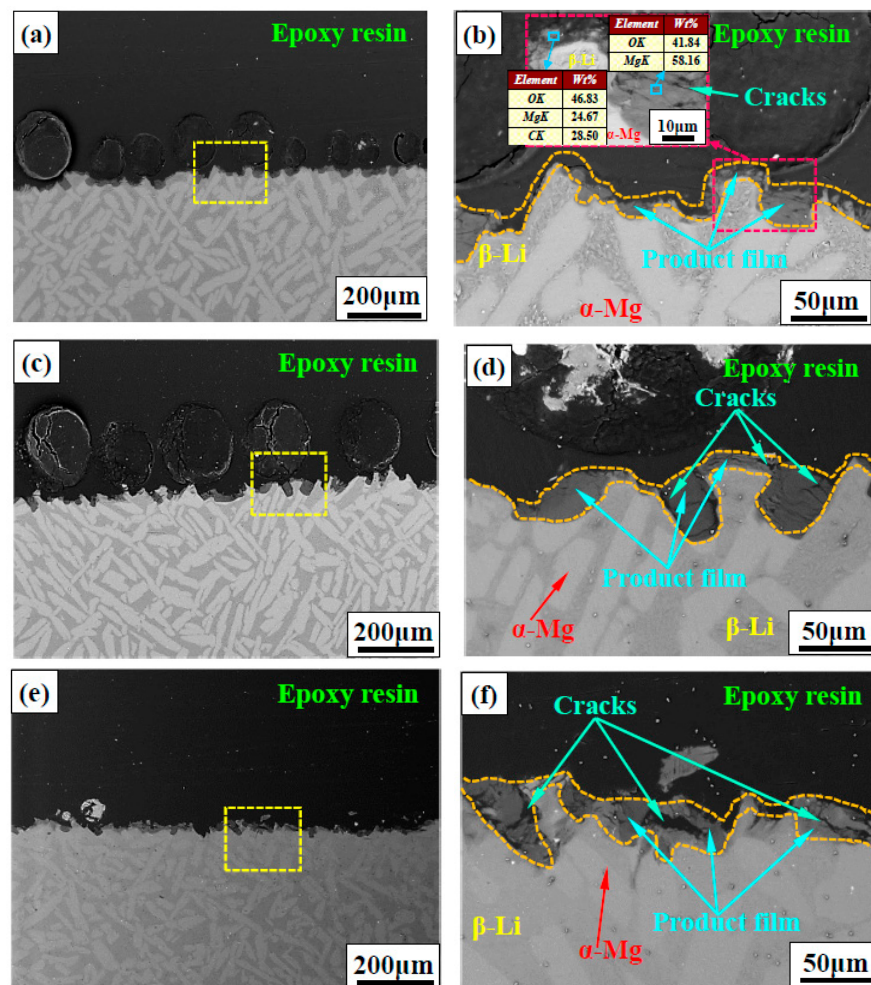


Figure 5. Cross-sectional morphologies of different samples after being hydrogen charged for: (a) 3 h, (c) 6 h and (e) 18 h. Images (b), (d) and (f) are high-magnified observations of the squared areas in images (a), (c) and (e), respectively.

3.2. Electrochemical Measurements

The potentiodynamic polarization curves for the differently charged samples are exhibited in Figure 6. This figure showed that the anodic and cathodic branches of the curves were not symmetric. Generally, for the Mg alloys, the cathodic branch corresponded to the occurrence of hydrogen evolution, whereas the anodic branch was concerned with the anodic dissolution of the α -Mg matrix [36]. Due to the occurrence of a negative difference effect (NDE) and pitting during the potentiodynamic polarization tests, the anodic branch was not suitable for fitting [13,14,36,37]. Therefore, the measured corrosion parameters of the differently charged samples were fitted from the cathodic branches using Tafel extrapolation. The fitting results are listed in Table 2. The results revealed that the corrosion potentials (E_{corr}) of the differently charged samples were basically the same (about -1.60 V_{SCE}) and the corrosion current density (i_{corr}) values of the 0, 3, 6 and 18 h charged samples were 51.9, 17.1, 18.2 and 19.1 $\mu\text{A}/\text{cm}^2$, respectively, indicating that the corrosion resistance of the Mg-8%Li alloy could be promoted by hydrogen charging. However, it should be noted that with the hydrogen charging time being prolonged from 3 to 18 h, the corrosion resistance of the alloy decreased slightly. Moreover, for the charged samples, an obvious film breakdown potential at about -1.45 V_{SCE} could be observed in their anodic branches.

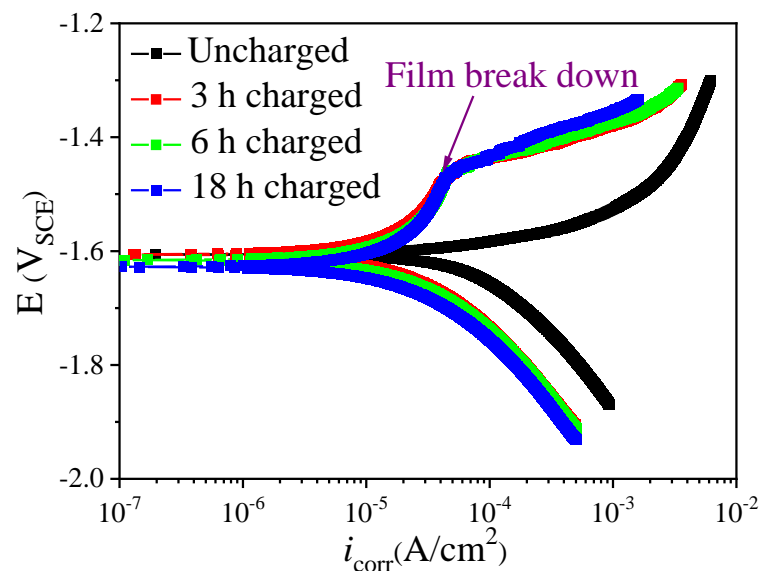


Figure 6. Potentiodynamic polarization curves of differently charged samples measured in a 0.1 M NaCl solution.

Table 2. Fitting results from the polarization curves of differently charged samples measured in a 0.1 M NaCl solution.

Hydrogen Charging Time (h)	i_{corr} ($\mu\text{A}/\text{cm}^2$)	E_{corr} (V _{SCE})
0	51.9 ± 8.1	-1.61 ± 0.01
3	17.1 ± 0.1	-1.61 ± 0.01
6	18.2 ± 0.3	-1.62 ± 0.01
18	19.1 ± 0.7	-1.62 ± 0.01

The EIS plots of the different samples are shown in Figure 7. The spectrum of the uncharged sample was composed of a high-frequency capacitive loop and a low-frequency inductive loop (Figure 7a). Generally, the low-frequency inductive loop was correlated with the occurrence of localized corrosion [16]. For the charged samples, the plots had a single capacitive loop and the impedance gradually decreased with the increase in charging

time. Moreover, in order to fit the EIS plots, two kinds of equivalent circuits were employed (Figure 7b,c) and the fitting results are listed in Table 3. The equivalent circuit in the uncharged sample consisted of the solution resistance (R_s), charge-transfer resistance (R_{ct}) and the double-layer capacitance at the alloy matrix/electrolyte interface (Q_{dl}) in the high-frequency capacitance loop, and the inductive resistance (R_L) and inductance (L) in the low-frequency inductance loop [16]. For the charged samples, the equivalent circuit was composed of the R_s , R_{ct} and Q_{dl} . Among them, the Q_{dl} was used to replace the ideal capacitor and account for the heterogeneity in the system [6,14]. Moreover, the Q_{dl} could be defined as Y_{dl} and n_{dl} , where n_{dl} is the dispersion coefficient [6,14]. Generally, the Q_{dl} was regarded as a capacitor when the n_{dl} value was 1 and could serve as the resistance when the n_{dl} value was 0 [6,13]. This finding revealed that when the hydrogen charging time was prolonged from 0 to 3 h, the determined R_{ct} values of the alloy increased from 527 to 1219 $\Omega\cdot\text{cm}^2$. After being hydrogen charged for 6 and 18 h, the R_{ct} values were slightly decreased to 1147 and 1039 $\Omega\cdot\text{cm}^2$, respectively.

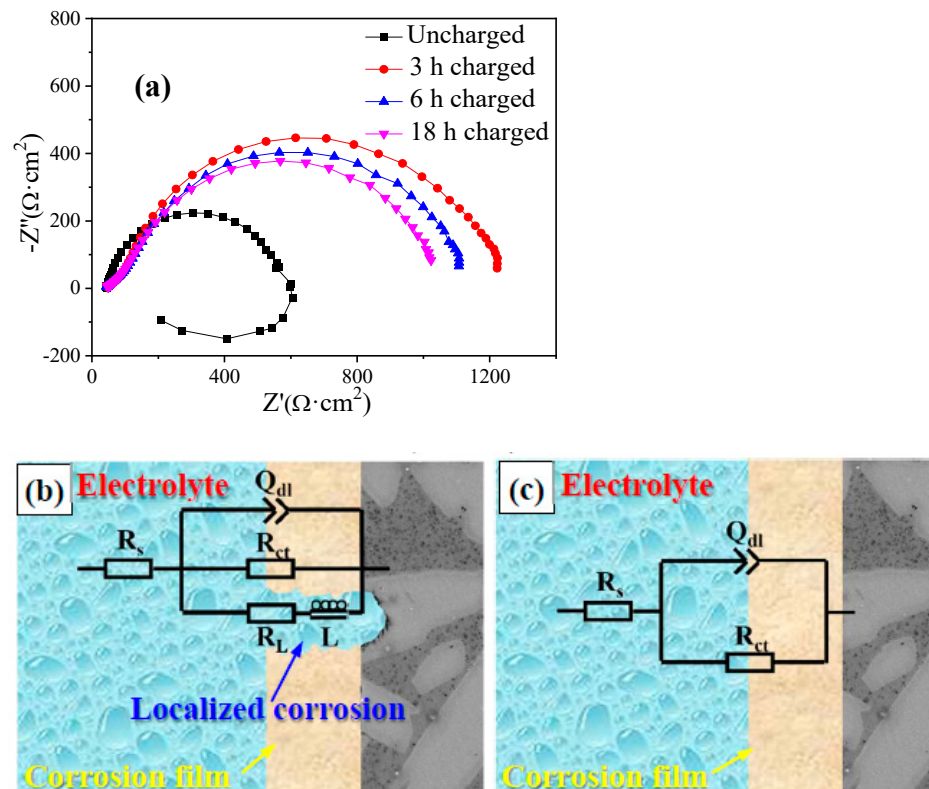


Figure 7. Nyquist plots and equivalent circuits of differently charged samples measured in a 0.1 M NaCl solution: (a) Nyquist plots, (b) equivalent circuit of uncharged sample and (c) equivalent circuit of 3, 6 and 18 h charged samples.

Table 3. The fitting EIS data of differently charged samples based on the equivalent circuits.

Hydrogen Charging Time (h)	R_s ($\Omega\text{ cm}^2$)	Y_{dl} (μF)	n_{dl}	R_{ct} ($\Omega\text{ cm}^2$)	L (H cm^{-2})	R_L ($\Omega\text{ cm}^2$)
0	42 ± 1	36.9 ± 3.6	0.88 ± 0.01	527 ± 22	3411 ± 854	256 ± 16
3	43 ± 2	24.3 ± 1.3	0.90 ± 0.01	1219 ± 40	-	-
6	46 ± 3	39.9 ± 1.5	0.87 ± 0.01	1147 ± 83	-	-
18	46 ± 7	31.8 ± 0.2	0.88 ± 0.01	1039 ± 62	-	-

3.3. Hydrogen Evolution

The hydrogen evolution curves of the differently charged samples immersed in a 0.1 M NaCl solution are presented in Figure 8. Following the gradients of the different curves, the results of the hydrogen evolution rates in the 3, 6 and 18 h charged samples were similar and were about 0.67 times lower than that of the uncharged sample. Since the electrochemical corrosion rates of the Mg–Li alloys were always proportional to the hydrogen evolution rates when immersed in the NaCl solution at OCP [13,14,17], this proved that the charged samples had the higher corrosion resistance, which was broadly consistent with the polarization and EIS data (Figures 6 and 7).

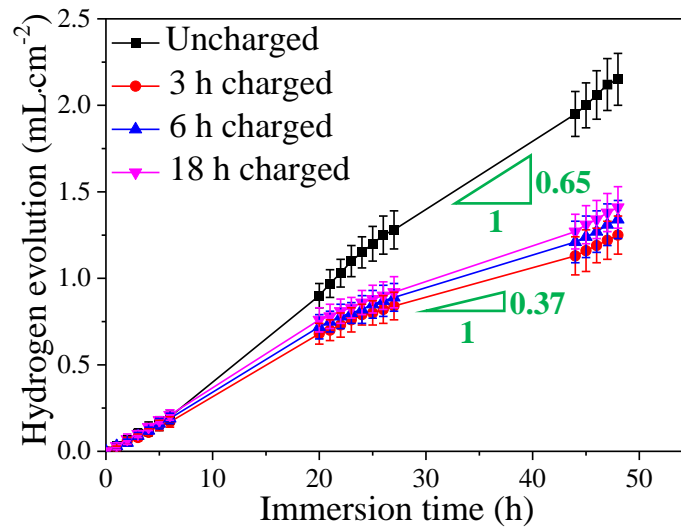


Figure 8. Hydrogen evolution curves of differently charged samples measured in a 0.1 M NaCl solution.

3.4. Corrosion Morphology

The macro corroded surfaces of the uncharged and 3 h charged samples immersed in the 0.1 M NaCl solution for different durations are exhibited in Figure 9. The results showed that for the uncharged sample, the localized corrosion mainly occurred at the edges of the sample when immersed for 2 h. The corroded area was significantly increased as the immersion time was prolonged. After being immersed for 48 h, substantial corrosion products almost covered the whole sample surface. In the 3 h charged sample, when the immersion time was less than 24 h, no obvious localized corrosion could be observed on the surface, demonstrating that the hydrogen-charged sample had a high corrosion performance in the NaCl solution. After being immersed for 48 h, the localized corrosion only occurred at the edges of the sample.

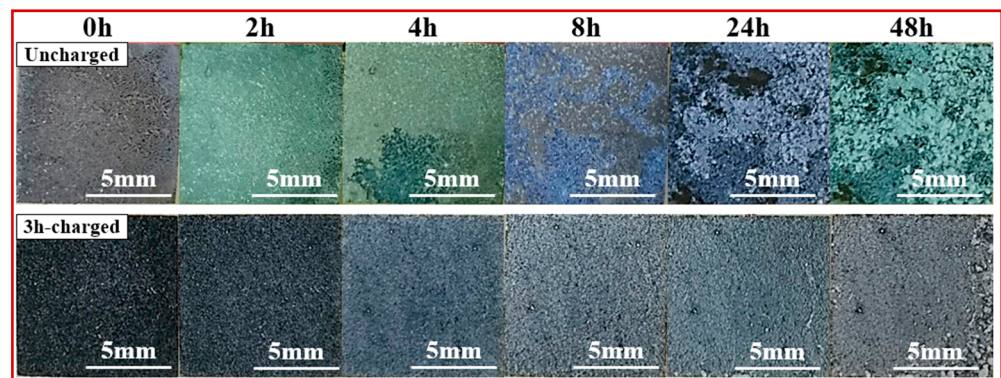


Figure 9. Macro corroded surfaces of the uncharged and 3 h charged samples after being immersed in the 0.1 M NaCl solution for different durations.

Figures 10 and 11, respectively, present the in situ observations of the evolution of the corroded regions on the surfaces of the uncharged and 3 h charged samples immersed for 2, 4 and 8 h in the 0.1 M NaCl solution. For the uncharged sample, at the early stage of corrosion, pits preferentially occurred at the α -Mg/ β -Li interphases and in the α -Mg phase. The maximum surface height difference was almost unchanged (Figure 10c,d). After being immersed for 4 h, obvious localized corrosion propagated from the α -Mg phase to the β -Li phase and the maximum surface height difference due to the formed corrosion products was reached at 20.56 μ m (Figure 10e,f). When the sample was immersed for 8 h, the corrosion severity further intensified and the maximum surface height difference of the localized corrosion was 35.87 μ m (Figure 10g,h).

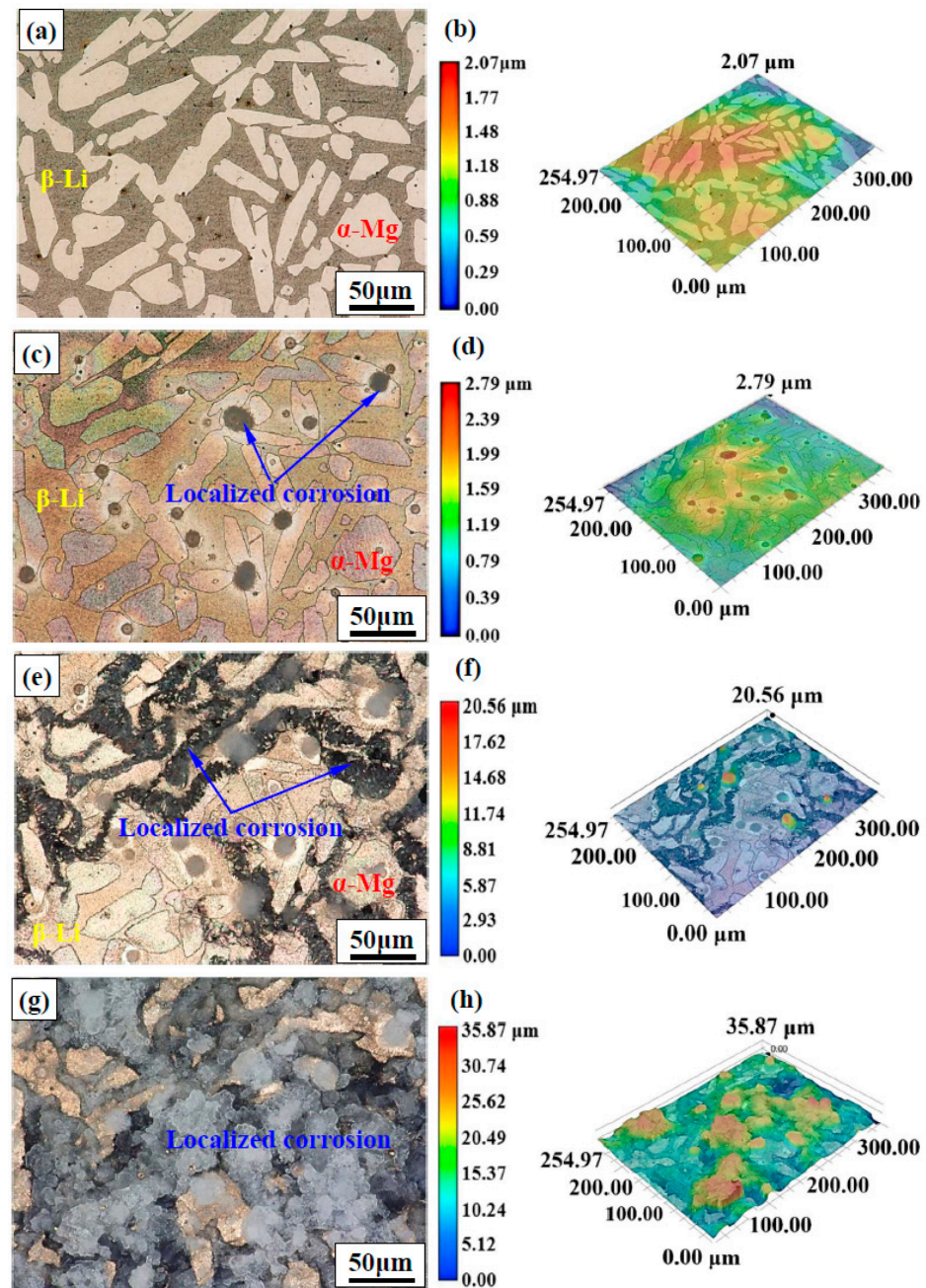


Figure 10. Surface corrosion morphologies and 3D images of the uncharged sample after being immersed in a 0.1 M NaCl solution for: (a) 0 h, (c) 2 h, (e) 4 h and (g) 8 h. Images (b), (d), (f) and (h) are the corresponding 3D morphologies of images (a), (c), (e) and (g), respectively.

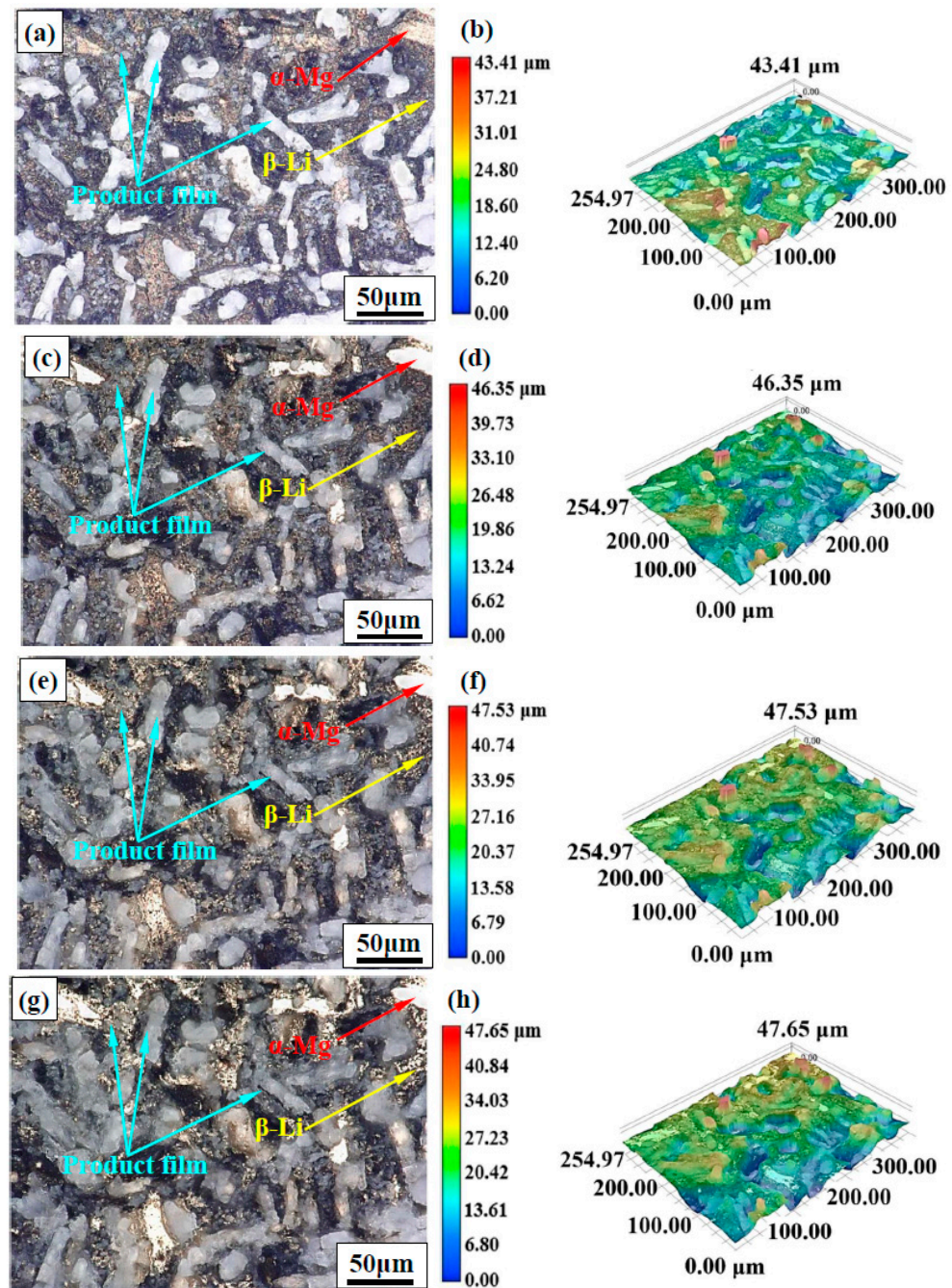


Figure 11. Surface corrosion morphologies and 3D images of the 3 h charged sample after being immersed in a 0.1 M NaCl solution for: (a) 0 h, (c) 2 h, (e) 4 h and (g) 8 h. Images (b), (d), (f) and (h) are the corresponding 3D morphologies of images (a), (c), (e) and (g), respectively.

In the 3 h charged sample, obvious product films were formed in the two matrix phases and the maximum surface height difference was 43.41 μm (Figure 11a,b). With the immersion time being prolonged from 2 to 8 h, no obvious localized corrosion occurred on the sample surface and the maximum surface height difference was slightly increased from 46.35 to 47.65 μm (Figure 11c–h), indicating that the product films being formed in the two matrix phases of the 3 h charged sample exhibited good corrosion protectiveness.

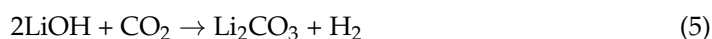
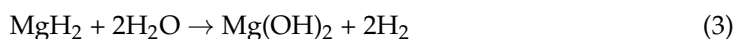
4. Discussion

In this study, the corrosion resistance of an Mg–8%Li alloy was effectively improved after hydrogen charging (Figures 6–8). Previous work demonstrated that for hydrogen-

charged Mg alloys, the change of their corrosion behavior was related to the formation of product films during the hydrogen charging process [17,29–32]. Therefore, in order to disclose the mechanism for improving corrosion resistance in the charged Mg–8%Li alloy, it was necessary to investigate the components and formation mechanisms of the formed product films in two matrix phases. Based on the Pourbaix diagram of the Mg–H₂O system, when the applied potential was lower than $-2.36 V_{SCE}$, the anodic dissolution of Mg could not occur in a neutral solution at 25 °C and an atmosphere of 1 atm [38]. Similarly, on the basis of the Pourbaix diagram of the Li–H₂O system in a neutral solution at 25 °C and an atmosphere of 1 atm, it was revealed that Li could not be corroded when the applied potential was lower than $-3.25 V_{SCE}$ [39]. In the current investigation, since the applied charging potential was $-4.50 V_{SCE}$, the anodic dissolution in the α -Mg and β -Li phases could not occur during the hydrogen charging process. Therefore, the formation of the product films in the two matrix phases could be induced by hydrogen charging. Previous research reported that Mg and Li could react with charged hydrogen to form MgH₂ [38] and LiH hydrides [40], which are expressed in Reaction (1) and Reaction (2), respectively:



However, MgH₂ and LiH could be easily decomposed into Mg(OH)₂ and LiOH and generate H₂ when exposed to water [38,41], as expressed in Reaction (3) and Reaction (4). Moreover, LiOH could react with CO₂ in the air to form Li₂CO₃ [42], as expressed in Reaction (5):



Therefore, it could be inferred that for the charged Mg–8%Li alloy, the formed product film in the α -Mg phase should mainly consist of Mg(OH)₂ (Figure 5) originating from the hydrolysis of the MgH₂ hydrides. Moreover, the product film in the β -Li phase should be composed of LiOH and Li₂CO₃, and the presence of Li₂CO₃ could be ascribed to the transformation of LiOH during long-time exposure to the air after the hydrogen charging processes. It was interesting to note that the thicknesses of the product films in the α -Mg phase were much larger than those in the β -Li phase for the differently charged samples (Figure 5). The main reason was that for the dual-phase structured Mg–Li alloys, the corrosion potentials in the α -Mg and β -Li phases were $-1.75 V_{SCE}$ and $-2.38 V_{SCE}$ [34], respectively, and the driving force for hydrogen evolution in the α -Mg phase was much stronger than that in β -Li phase under the same applied hydrogen charging potential of $-4.50 V_{SCE}$. This could lead to the formation of more product films in the α -Mg phase (Figure 5). It has been reported that when dual-phase Mg–Li alloys were immersed in a NaCl solution, the main component of the product film formed in the α -Mg phase was Mg(OH)₂ [6,13,14]. However, the Cl[−] could react with the Mg(OH)₂ film to form MgCl₂, resulting in the degraded protectiveness of the Mg(OH)₂ film in the α -Mg phase [13,14]. For to this reason, Li et al. [6] reported that after being immersed in a 0.1 M NaCl solution for 4 h, the R_{ct} of the Mg–7.5Li alloy was reduced by 62% and pits mainly initiated in the α -Mg phase. However, in the current work, the R_{ct} of the Mg–8%Li alloy was increased by 57% after being hydrogen charged for 3 h (Figure 7). Furthermore, the product film in the α -Mg phase could effectively prevent the occurrence of localized corrosion after being immersed in the 0.1 M NaCl solution for 8 h (Figure 11). Therefore, it could be inferred that the Mg(OH)₂ film being formed by electrochemical hydrogen charging had a good corrosion performance in the NaCl solution. Wu et al. [43] reported that a dense

Mg(OH)₂ film, which could hinder the erosion of Cl⁻, could be prepared on the surface of the AZ91D alloy using cathodic polarization. Thus, it could be conjectured that a Mg(OH)₂ film being prepared using a similar cathodic polarization method should also have the dense structure and the strong corrosion protectability. In addition to the product film in the α-Mg phase, the product film being formed in the β-Li phase also had good corrosion protectiveness (Figure 11). As mentioned previously, the product film in the β-Li phase should be constituted by LiOH and Li₂CO₃. However, for dual-phase Mg–Li alloys, Mg could exist in the β-Li phase as the solid solute [6]. Thus, it could be found that a small amount of Mg(OH)₂ could be formed in the β-Li phase during the hydrogen charging process. Zhang et al. [44] reported that the mixture of LiOH/Mg(OH)₂ could effectively promote the corrosion resistance of a Li–Mg electrode. Similarly, it could be speculated that the β-Li phase could also be protected by the LiOH/Mg(OH)₂ film. Moreover, Xu et al. [45] reported that a BCC structured Mg–10.95%Li–3.29%Al–0.59%Y–0.19%Zr alloy could have superior corrosion resistance due to the formation of the protective Li₂CO₃ film on the surface. Thus, it could be deduced that the Li₂CO₃ film in the β-Li phase should also have similarly high corrosion protectability.

However, it should be noted that the corrosion resistance of the charged samples gradually decreased with prolonged hydrogen charging time (Figures 6–8). The SEM observations of the cross-sections of the charged samples revealed that when the hydrogen charging time was prolonged, the number of cracks being presented in the interior of the surface product films and at the interfaces of the product film/substrate phases would be increased (Figure 5). In a previous study, Chen et al. [31] reported that during the hydrogen charging process of an AZ91 Mg alloy, the charged hydrogen atoms could combine into the H₂ gas in the interior of the corrosion film and react with the alloy matrix to form hydride. With the increase in hydrogen charging time, the hydrogen pressure induced by the H₂ gas and expansion stress caused by the formation of the hydrides could lead to the rupture of the corrosion film and degrade the corrosion resistance. Similarly, it can be speculated that for the charged Mg–8%Li alloy, cracking of the product film in the α-Mg phase should also be attributed to the formation of H₂ gas and hydrides. Moreover, it has been reported that the Pilling–Bedworth ratios (PBR) of the Mg(OH)₂, LiOH and Li₂CO₃ films were all larger than 1 [46], indicating that they had a larger volume than the Mg–Li matrix and their formation could induce local stresses [47]. Thus, for the sample being charged for a longer time, the gradually increased local stresses in the product films and at the product film/substrate phases could further promote the formation of cracks and degrade the corrosion protectability of the product films. In addition, previous studies demonstrated that although the yield strength, ultimate tensile strength and the elongation ratio to failure of the investigated Mg–8%Li alloy were gradually decreased with the increase in hydrogen charging time, the elongation ratio to failure of the alloy could still be 12.4 % even after being hydrogen charged at the cathodic current density of 50 mA/cm² for 18 h. This indicated that the Mg–8%Li alloy had a high resistance to hydrogen embrittlement [33]. Combined with the beneficial effect of hydrogen charging on the improvement of corrosion performance, this demonstrated that the Mg–8%Li alloy could be used as a candidate material in the hydrogen-containing service environment.

5. Conclusions

In this study, the effect of a product film formed by electrochemical hydrogen charging on the corrosion behavior of an as-cast Mg–8%Li alloy was investigated. The main conclusions were as follows:

- (1) After being hydrogen charged at 50 mA/cm² for 3 h in a 0.1 M NaCl solution, an obvious product film composed of Mg(OH)₂, LiOH and Li₂CO₃ was formed in the two matrix phases of the Mg–8%Li alloy. Moreover, the thickness values of the formed product films in both of the phases increased with the prolongation of the hydrogen charging time.
- (2) After being hydrogen-charged for 3 h, the formed product films in both of the two matrix phases were dense and had a high corrosion resistance in the NaCl solution.

Therefore, the matrix of the Mg–8%Li alloy underneath the product films could be protected. However, when the hydrogen charging time was increased to 18 h, the protectiveness of the product films was weakened because the number of cracks being presented in the interior of the films and at the interfaces of the product film/substrate phases was increased.

Author Contributions: Conceptualization, D.X. and S.W.; methodology, S.W.; software, S.W. and X.X.; validation, D.X., Z.Z. and B.W.; formal analysis, S.W. and D.W.; investigation, S.W.; resources, D.X.; data curation, D.X. and S.W.; writing—original draft preparation, S.W.; writing—review and editing, D.X., B.W. and S.W.; visualization, S.W., D.W. and X.X.; supervision, D.X.; project administration, D.X. and B.W.; funding acquisition, D.X. and Z.Z. All authors have read and agreed to the published version of the manuscript.

Funding: This research was supported by the National Natural Science Foundation of China Projects under Grant [Nos. U21A2049, 52071220, 51871211, 51701129 and 51971054], Liaoning Province's project of "Revitalizing Liaoning Talents" (XLYC1907062), the Doctor Startup Fund of the Natural Science Foundation of Liaoning Province (No. 2019-BS-200), the Strategic New Industry Development Special Foundation of Shenzhen (JCYJ20170306141749970), the funds of the International Joint Laboratory for Light Alloys, Liaoning BaiQianWan Talents Program, the Domain Foundation of Equipment Advance Research of the 13th Five-Year Plan (61409220118), the National Key Research and Development Program of China under Grant [Nos. 2017YFB0702001 and 2016YFB0301105], the Innovation Fund of the Institute of Metal Research (IMR), the Chinese Academy of Sciences (CAS), the National Basic Research Program of China (973 Program) project under Grant No. 2013CB632205 and the Fundamental Research Fund for the Central Universities under Grant [No. N2009006], Bintechn-IMR R&D Program [No. GYY-JSBU-2022-009].

Institutional Review Board Statement: Not applicable.

Informed Consent Statement: Not applicable.

Data Availability Statement: Not applicable.

Conflicts of Interest: The authors declare no conflict of interest.

References

1. Wu, R.; Yan, Y.; Wang, G.; Murr, L.E.; Han, W.; Zhang, Z.; Zhang, M. Recent progress in magnesium-lithium alloys. *Int. Mater. Rev.* **2015**, *60*, 65–100. [[CrossRef](#)]
2. Yang, Y.; Xiong, X.M.; Chen, J.; Peng, X.D.; Chen, D.L.; Pan, F.S. Research advances in magnesium and magnesium alloys worldwide in 2020. *J. Magnes. Alloy.* **2021**, *9*, 705–747. [[CrossRef](#)]
3. Hou, J.Y.; Wang, B.J.; Xu, D.K.; Cui, L.J.; Sun, J. Effect of surfactants on the corrosion protectability of calcium phosphate conversion coatings on duplex structured Mg-8Li (in wt. %) alloy. *Coatings* **2022**, *12*, 1182. [[CrossRef](#)]
4. Wang, B.J.; Hou, J.Y.; Luan, J.Y.; Xu, D.K.; Sun, H.J.; Sun, J. The corrosion behaviors of an as-rolled Mg-8Li (in wt. %) alloy in two differently concentrated NaCl Solutions. *Coatings* **2022**, *12*, 406. [[CrossRef](#)]
5. Estrin, Y.; Nene, S.S.; Kashyap, B.P.; Prabhu, N.; Samman, T.A. New hot rolled Mg-4Li-1Ca alloy: A potential candidate for automotive and biodegradable implant applications. *Mater. Lett.* **2016**, *173*, 252–256. [[CrossRef](#)]
6. Li, C.Q.; Xu, D.K.; Chen, X.B.; Wang, B.J.; Wu, R.Z.; Han, E.H.; Birbilis, N. Composition and microstructure dependent corrosion behaviour of Mg-Li alloys. *Electrochim. Acta* **2018**, *260*, 55–64. [[CrossRef](#)]
7. Zhong, F.; Wu, H.J.; Jiao, Y.L.; Wu, R.Z.; Zhang, J.H.; Hou, L.G.; Zhang, M.L. Effect of Y and Ce on the microstructure, mechanical properties and anisotropy of as-rolled Mg-8Li-1Al alloy. *J. Mater. Sci. Technol.* **2020**, *39*, 124–134. [[CrossRef](#)]
8. Li, C.Q.; Xu, D.K.; Wang, B.J.; Sheng, L.Y.; Qiao, Y.X.; Han, E.H. Natural ageing responses of duplex structured Mg-Li based alloys. *Sci. Rep.* **2017**, *7*, 40078. [[CrossRef](#)]
9. Xu, D.K.; Li, C.Q.; Wang, B.J.; Han, E.H. Effect of icosahedral phase on the crystallographic texture and mechanical anisotropy of duplex structured Mg-Li alloys. *Mater. Des.* **2015**, *88*, 88–97. [[CrossRef](#)]
10. Xu, D.K.; Zu, T.T.; Yin, M.; Han, E.H. Mechanical properties of the icosahedral phase reinforced duplex Mg-Li alloy both at room and elevated temperatures. *J. Alloys Compd.* **2014**, *582*, 161–166. [[CrossRef](#)]
11. Xu, D.K.; Liu, L.; Xu, Y.B.; Han, E.H. The strengthening effect of icosahedral phase on as-extruded Mg-Li alloys. *Scr. Mater.* **2007**, *57*, 285–288. [[CrossRef](#)]
12. Dobkowska, A.; Adamczyk-Cieślak, B.; Kubásek, J.; Vojtěch, D.; Kuc, D.; Hadasik, E.; Mizera, J. Microstructure and corrosion resistance of a duplex structured Mg-7.5Li-3Al-1Zn. *J. Magnes. Alloy.* **2021**, *9*, 467–477. [[CrossRef](#)]
13. Wang, B.J.; Xu, D.K.; Cai, X.; Qiao, Y.X.; Sheng, L.Y. Effect of rolling ratios on the microstructural evolution and corrosion performance of an as-rolled Mg-8 wt. %Li alloy. *J. Magnes. Alloy.* **2021**, *9*, 560–568. [[CrossRef](#)]

14. Wang, B.J.; Xu, K.; Xu, D.K.; Cai, X.; Qiao, Y.X.; Sheng, L.Y. Anisotropic corrosion behavior of hot-rolled Mg-8 wt. %Li alloy. *J. Mater. Sci. Technol.* **2020**, *53*, 102–111. [[CrossRef](#)]
15. Song, Y.W.; Shan, D.Y.; Chen, R.S.; Han, E.H. Corrosion characterization of Mg-8Li alloy in NaCl solution. *Corros. Sci.* **2009**, *51*, 1087–1094. [[CrossRef](#)]
16. Wang, S.D.; Xu, D.K.; Wang, B.J.; Sheng, L.Y.; Han, E.H.; Dong, C. Effect of solution treatment on stress corrosion cracking behavior of an as-forged Mg-Zn-Y-Zr alloy. *Sci. Rep.* **2016**, *6*, 29471. [[CrossRef](#)]
17. Wang, S.D.; Xu, D.K.; Wang, B.J.; Sheng, L.Y.; Qiao, Y.X.; Han, E.H.; Dong, C. Influence of phase dissolution and hydrogen absorption on the corrosion behavior of Mg-7%Gd-5%Y-1%Nd-0.5%Zr alloy in 3.5 wt. % NaCl solution. *Corros. Sci.* **2018**, *142*, 185–200. [[CrossRef](#)]
18. Chen, J.; Wang, J.Q.; Han, E.H.; Ke, W. Effect of hydrogen on stress corrosion cracking of magnesium alloy in 0.1 M Na₂SO₄ solution. *Mater. Sci. Eng. A* **2008**, *488*, 428–434. [[CrossRef](#)]
19. Chen, J.; Wang, J.Q.; Han, E.H.; Ke, W. Electrochemical corrosion and mechanical behaviors of the charged magnesium. *Mater. Sci. Eng. A* **2008**, *494*, 257–262. [[CrossRef](#)]
20. Uematsu, Y.; Kakiuchi, T.; Nakajima, M. Stress corrosion cracking behavior of the wrought magnesium alloy AZ31 under controlled cathodic potentials. *Mater. Sci. Eng. A* **2012**, *531*, 171–177. [[CrossRef](#)]
21. Sozanska, M.; Moscicki, A. Investigation of the susceptibility of the WE54 Magnesium based alloy to stress corrosion cracking. *J. Mater. Eng. Perform.* **2020**, *29*, 949–963. [[CrossRef](#)]
22. Dubey, D.; Kadali, K.; Panda, S.S.; Kumar, A.; Jain, J.; Mondal, K.; Singh, S.S. Comparative study on the stress corrosion cracking susceptibility of AZ80 and AZ31 magnesium alloys. *Mater. Sci. Eng. A* **2020**, *792*, 139793. [[CrossRef](#)]
23. Merson, E.; Myagkikh, P.; Poluyanov, V.; Merson, D.; Vinogradov, A. On the role of hydrogen in stress corrosion cracking of magnesium and its alloys: Gas-analysis study. *Mater. Sci. Eng. A* **2019**, *748*, 337–346. [[CrossRef](#)]
24. Zhou, L.F.; Liu, Z.Y.; Wu, W.; Li, X.G.; Du, C.W.; Jiang, B. Stress corrosion cracking behavior of ZK60 magnesium alloy under different conditions. *Int. J. Hydrog. Energy* **2017**, *42*, 26162–26174. [[CrossRef](#)]
25. Shi, Z.M.; Hofstetter, J.; Cao, F.Y.; Uggowitzer, P.J.; Dargusch, M.S.; Atrens, A. Corrosion and stress corrosion cracking of ultra-high-purity Mg₅Zn. *Corros. Sci.* **2015**, *93*, 330–335. [[CrossRef](#)]
26. Wang, S.; Xu, D.K.; Wang, D.L.; Zhang, Z.Q.; Wang, B.J. Effect of icosahedral phase formation on the stress corrosion cracking (SCC) behaviors of the as-cast Mg-8%Li (in wt. %) based alloys. *J. Magnes. Alloy.* **2022**; *in press*. [[CrossRef](#)]
27. Kappes, M.; Iannuzzi, M.; Carranza, R.M. Hydrogen embrittlement of magnesium and magnesium alloys: A review. *J. Electrochem. Soc.* **2013**, *160*, C168–C178. [[CrossRef](#)]
28. Lynch, S. Hydrogen embrittlement phenomena and mechanisms. *Corros. Rev.* **2012**, *30*, 105–123. [[CrossRef](#)]
29. Zhang, T.; Shao, Y.W.; Meng, G.Z.; Li, Y.; Wang, F.H. Effects of hydrogen on the corrosion of pure magnesium. *Electrochim. Acta* **2006**, *52*, 1323–1328. [[CrossRef](#)]
30. Zhang, T.; Li, Y.; Wang, F.H. Roles of β phase in the corrosion process of AZ91D magnesium alloy. *Corros. Sci.* **2006**, *48*, 1249–1264. [[CrossRef](#)]
31. Chen, J.; Wang, J.Q.; Han, E.H.; Dong, J.H.; Ke, W. States and transport of hydrogen in the corrosion process of an AZ91 magnesium alloy in aqueous solution. *Corros. Sci.* **2008**, *50*, 1292–1305. [[CrossRef](#)]
32. Song, Y.W.; Han, E.H.; Dong, K.H.; Shan, D.Y.; Yim, C.D.; You, B.S. Effect of hydrogen on the corrosion behavior of the Mg-xZn alloys. *J. Magnes. Alloy.* **2014**, *2*, 208–213. [[CrossRef](#)]
33. Wang, S.; Xu, D.K.; Wang, D.L.; Zhang, Z.Q.; Liu, L.; Wang, B.J. Effect of electrochemical hydrogen charging on the microstructure and mechanical behavior of an as-cast Mg-8%Li (in wt. %) alloy. *J. Magnes. Alloy.* **2023**; *to be submitted*.
34. Morishige, T.; Doi, H.; Goto, T.; Nakamura, E.; Takenaka, T. Exfoliation Corrosion Behavior of Cold-Rolled Mg-14 mass% Li-1 mass% Al Alloy in NaCl Solution. *Mater. Trans.* **2013**, *54*, 1863–1866. [[CrossRef](#)]
35. Li, C.Q.; Deng, B.B.; Dong, L.J.; Shi, B.Q.; Dong, Y.; Peng, F.; Zhang, Z.R. Effect of Zn addition on the corrosion behaviours of as-cast BCC Mg-11Li based alloys in NaCl solution. *Mater. Design* **2022**, *221*, 111019. [[CrossRef](#)]
36. Atrens, A.D.; Gentle, I.; Atrens, A. Possible dissolution pathways participating in the Mg corrosion reaction. *Corros. Sci.* **2015**, *92*, 173–181. [[CrossRef](#)]
37. Zhao, M.C.; Liu, M.; Song, G.L.; Atrens, A. Influence of pH and chloride ion concentration on the corrosion of Mg alloy ZE41. *Corros. Sci.* **2008**, *50*, 3168–3178. [[CrossRef](#)]
38. Chen, J.; Dong, J.H.; Wang, J.Q.; Han, E.H.; Ke, W. Effect of magnesium hydride on the corrosion behavior of an AZ91 magnesium alloy in sodium chloride. *Corros. Sci.* **2008**, *50*, 3610–3614. [[CrossRef](#)]
39. Pourbaix, M. Atlas of electrochemical equilibria in aqueous solutions. *J. Electroanal. Chem.* **1967**, *13*, 471. [[CrossRef](#)]
40. Thakur, C.; Balasubramaniam, R. Hydrogen embrittlement of aged and retrogressed-reaged Al-Li-Cu-Mg alloys. *Acta Mater.* **1997**, *45*, 1323–1332. [[CrossRef](#)]
41. Dinh, L.N.; Grant, D.M.; Schildbach, M.A.; Smith, R.A.; Siekhaus, W.J.; Balazs, B.; Leckey, J.H.; Kirkpatrick, J.R.; McLean II, W. Kinetic measurement and prediction of the hydrogen outgassing from the polycrystalline LiH/Li₂O/LiOH system. *J. Nucl. Mater.* **2005**, *347*, 31–43. [[CrossRef](#)]
42. Cho, Y.M.; Lee, J.Y.; Bokare, A.D.; Kwon, S.B.; Park, D.S.; Jung, W.S.; Choi, J.S.; Yang, Y.M.; Lee, J.Y.; Choi, W.Y. LiOH-embedded zeolite for carbon dioxide capture under ambient conditions. *J. Ind. Eng. Chem.* **2015**, *22*, 350–356. [[CrossRef](#)]

43. Wu, F.X.; Li, W.X.; Liang, J. Electrochemical deposition and corrosion resistance of Mg(OH)₂ films on magnesium alloy. *Chin. J. Mater. Res.* **2014**, *28*, 703–709.
44. Zhang, Z.Y.; Chen, K.H.; Ni, E.F. Effect of magnesium on the electrochemical behavior of lithium anode in LiOH aqueous solution used for lithium-water battery. *Electrochim. Acta* **2010**, *55*, 3830–3837. [[CrossRef](#)]
45. Xu, W.Q.; Birbilis, N.; Sha, G.; Wang, Y.; Daniels, J.; Xiao, Y.; Ferry, M. A high-specific-strength and corrosion-resistant magnesium alloy. *Nat. Mater.* **2015**, *14*, 1229–1235. [[CrossRef](#)]
46. Zeng, R.C.; Sun, L.; Zheng, Y.F.; Cui, H.Z.; Han, E.H. Corrosion and characterisation of dual phase Mg-Li-Ca alloy in Hank's solution: The influence of microstructural features. *Corros. Sci.* **2014**, *79*, 69–82. [[CrossRef](#)]
47. Chen, J.; Ai, M.R.; Wang, J.Q.; Han, E.H.; Ke, W. Formation of hydrogen blister on AZ91 magnesium alloy during cathodic charging. *Corros. Sci.* **2009**, *51*, 1197–1200. [[CrossRef](#)]

Disclaimer/Publisher's Note: The statements, opinions and data contained in all publications are solely those of the individual author(s) and contributor(s) and not of MDPI and/or the editor(s). MDPI and/or the editor(s) disclaim responsibility for any injury to people or property resulting from any ideas, methods, instructions or products referred to in the content.